Interannual variations of the Hawaiian Lee Countercurrent induced by potential vorticity variability in the subsurface

Hideharu Sasaki[1*], Shang-Ping Xie[2], Bunmei Taguchi[1], Masami Nonaka[3], Shigeki Hosoda[4], and Yukio Masumoto[3]

[1]Earth Simulator Center, JAMSTEC, 3173-25 Showa-machi, Kanazawa-ku, Yokohama, Kanagawa, 236-0001 Japan.

[2]International Pacific Research Center and Department of Meteorology, University of Hawaii at Manoa, 2525 Correa Rd. Honolulu, HI 96822, USA

[3]Research Institute for Global Change, JAMSTEC, 3173-25 Showa-machi, Kanazawa-ku, Yokohama, Kanagawa, 236-0001 Japan.

[4]Research Institute for Global Change, JAMSTEC, 2-15, Natsushima, Yokosuka, Kanagawa, 237-0061 Japan

Corresponding author:
Hideharu Sasaki
Earth Simulator Center, JAMSTEC, 3173-25 Showa-machi, Kanazawa-ku, Yokohama, Kanagawa, 236-0001 Japan.
Phone: +81-45-778-5843
Fax: +81-45-778-5492
E-mail: sasaki@jamstec.go.jp

Abstract

Interannual variations of the Hawaiian Lee Countercurrent (HLCC) in the 2000s were investigated using satellite and Argo profiling float observations. The satellite observed sea surface height shows that the geostrophic eastward current was anomalously strong to the west away from Hawaii in 2003 and 2005. However, the trade winds and the orographic wind curl dipole on the lee of Hawaii that drives the climatological mean HLCC were not particularly strong in these years, suggesting that the accelerations of the HLCC were not caused by the wind stress curl forcing around Hawaii and subsequent Rossby wave propagation. Using Argo observations, we found negative potential vorticity (PV) anomalies in the subsurface north of the HLCC in these two years. The pycnocline is lifted northward as low PV waters of different densities stack up in the vertical, and the HLCC is then accelerated via the thermal wind. The intensification and/or southward intrusion of the Eastern Subtropical Mode Water and Subtropical Mode Water seem to have induced negative PV anomalies in 2003 and 2005, respectively. Using high-resolution ocean simulations, we confirmed the migrations of PV anomalies and their contributions to the HLCC accelerations. Although the HLCC is located away from the cores of major mode waters, our results suggest that interannual variations of the HLCC are affected by those of mode waters.

Keywords: Hawaiian Lee Countercurrent, low potential vorticity water, interannual variations, high-resolution ocean simulation

1. Introduction

The Hawaiian Lee Countercurrent (HLCC), a narrow eastward current extending far west of the Hawaiian Islands, has been observed from surface drifters (Qiu et al., 1997; Flament et al., 1998) and hydrography (Kobashi and Kawamura, 2002). The HLCC is one of the eastward subtropical countercurrents (STCC) that exist in the North Pacific (e.g., Uda and Hasumuma, 1969; Kobashi et al. 2006) and flow against both the northeasterly trade winds and the broad westward North Equatorial Current (NEC).

Quasi-steady, broad trade winds prevail over the Hawaiian Islands, generating a number of mechanical wakes behind individual islands (Smith and Grubišic, 1993; Yang et al., 2008a, b). The individual wakes dissipate within a few hundred kilometers, and a broad wake with a meridional dipole of wind stress curl forms (Hafner and Xie, 2003). Using satellite observations and an ocean general circulation model (OGCM), Xie et al. (2001) proposed a generation mechanism for the climatological mean HLCC (hereafter referred to as the wind-driven mechanism), suggesting that the HLCC is a response to the orographic wake in the lee of Hawaii that occurs via Rossby wave propagation. Using an atmosphere-ocean coupled general circulation model (GCM), Sakamoto et al. (2004) succeeded in reproducing the HLCC and confirmed that the islands trigger the current.

Several factors complicate the westward propagation of Hawaii’s orographic effects in the form of Rossby waves. For example, eddy variability with a 100-day time scale west of 160°W along 19°N is likely generated by the instability of the vertically sheared NEC and HLCC (Yoshida et al., 2010). Yu et al. (2003) suggested that the westward extension of the HLCC is limited to the east of the dateline because of meso-scale eddies that extract energy from the mean flow.

The southern subtropical front (STF) along 19°N−21°N west of the dateline, which is distinct from the HLCC front, is one of three STFs defined using hydrographic data by Kobashi et al. (2006). The STFs are associated with large meridional gradients of isopycnal potential vorticity (PV) below the fronts. Theoretical (Kubokawa, 1999) and numerical (Kubokawa and Inui, 1999) studies have shown that an STCC forms with the STF as low PV waters of different density become vertically stacked north of the STF, which push up isopycnals in the lower density range. The southern STF results from the southward intrusion of Subtropical Mode Water (STMW; e.g. Bingham, 1992; Hanawa and Talley, 2001) and upper Central Mode Water (CMW; e.g. Hanawa and Talley, 2001) in the subtropical gyre (Aoki et al., 2002; Kobashi et al., 2006).

Seasonal HLCC variations, which are strong from summer to winter and weak in spring, are detected in hydrographic data (Kobashi and Kawamura, 2002). The seasonal HLCC variations are consistent with the wind-driven mechanism for climatological HLCC generation and with the seasonal cycle of the trade winds (Kobashi and Kawamura, 2002). Using satellite observations and a high-resolution OGCM, Sasaki et al. (2010) confirmed the hypothesis of the seasonal HLCC variations.

Considerable interannual variability of the HLCC, which was stronger in 2003 and 2005 than in other years, was found in geostrophic currents estimated from satellite observed sea surface height (SSH) by Sasaki et al. (2010). However, the trade winds were not strong in these years, and the HLCC accelerations were stronger away from Hawaii than near Hawaii, suggesting that the wind-driven mechanism forced by the wind curl dipole near Hawaii is not dominant in the HLCC accelerations. Sasaki et al. (2010) suggested from an analysis using an OGCM simulation that the HLCC acceleration in 2003 seems to be induced by the intrusion of lower PV water associated with the CMW than usual to the north of the HLCC. However, the hypothesis is still a matter of speculation. The contributions of low PV water to HLCC acceleration have not been studied quantitatively or examined in observational data.

The present study examines the interannual variations of HLCC and their mechanism near and away from Hawaii separately, using satellite and Argo profiling float observations from 2001 to 2008 with a focus on the HLCC accelerations in 2003 and 2005. We consider not only the wind-driven mechanism but also low PV water intrusions in the subsurface. To support the observations, a high-resolution OGCM is also used to examine variations of PV and those induced by a wind forcing around Hawaii. It is expected that this study will help understand effects of mode waters on ocean circulation and climate in the North Pacific through revealing relationships between mode waters and surface currents, including the HLCC. As in a recent research using a coupled GCM, mode waters induce variations of STCC and generate sea surface temperature anomalies along STCC, which in turn affect wind and precipitation (Xie et al. 2011).

The contents of this paper are as follows. Section 2 describes the observational data and high-resolution simulations performed using an OGCM. In Section 3, interannual variations of the HLCC from 2001 to 2008 are presented, and their mechanisms are investigated using satellite and profiling float observations. Section 4 examines how the mechanism works in a high-resolution simulation. Section 5 discusses how the intrusion of low PV water masses is induced and then suggests other possible mechanisms that could interannually accelerate the HLCC. Section 6 presents our conclusions.

2. Observations and a high-resolution OGCM simulation

2.1 Observational data

We examined satellite observations of SSH and surface wind stress to detect interannual variations of the HLCC and trade winds. Maps of Absolute Dynamic Topography (MADT) products were obtained from archiving and interpretation of satellite oceanographic data (AVISO; http://www.aviso.oceanobs. com). The SSH data every 7 days were constructed from multiple satellite altimetry data since 1993 with horizontal resolution of 0.25°. Daily mean surface wind stress data with horizontal grid of 0.5° based on Quick Scatterometer (QuikSCAT) satellite observations from July 1999 to October 2009 included in the Japanese Ocean Flux Data sets with the Use of Remote Sensing Observations product (J-OFURO, Kutsuwada, 1998; Kubota et al., 2002) were also used.

The monthly temperature and salinity data from 2001 with 1° horizontal resolution included in the MOAA GPV dataset (Grid Point Value of the Monthly Objective Analysis using Argo float data; Hosoda et al., 2008, http://www.jamstec.go.jp/ARGO/J_ARGOe.htm) were used to detect interannual variations in subsurface PV. The grid data product was constructed from not only Argo profiling float data but also data from the Triangle Trans-Ocean Buoy Network (TRITON) and available conductivity-temperature-depth (CTD) profilers. A two-dimensional optimal interpolation (OI) method is used to produce the grid data on pressure levels from 10 dbar to 2,000 dbar, and the first guess field is the monthly climatology data of the World Ocean Atlas 2001 (WOA01; Boyer et al., 2002; Stephens et al., 2002). The 10 dbar level is the first pressure level near the sea surface. We also used the potential density and dynamic height at 10 dbar referenced to 2,000 dbar in the MOAA GPV product. Interpolation errors related to the grid data for the North Pacific are not insignificant before 2002 owing to the small number of Argo profiling float observations (Hosoda et al., 2008). However, it is expected that the grid data capture the long-term mean and interannual variability of subsurface PV after 2003.

2.2 Hindcast and sensitivity simulations using an OGCM

Interannual PV variations from 2001 to 2008 were further examined using a high-resolution OGCM. We used the OGCM for the Earth Simulator (OFES; Masumoto et al., 2004) based on GFDL MOM3 (Modular Ocean Model 3 developed by Geophysical Fluid Dynamics Laboratory, Pacanowski and Griffies, 1999). The model domain is quasi-global from 75°S to 75°N, and the horizontal resolution is 0.1°, with 54 vertical levels. A hindcast simulation using the OFES is forced at the surface by daily mean QuikSCAT wind stress with a 1° horizontal resolution in the J-OFURO product (Kutsuwada, 1998; Kubota et al., 2002) and National Centers for Environmental Prediction/National Center for Atmospheric Research (NCEP/NCAR) reanalysis data (Kalnay et al., 1996) from July 1999 to 2008 (Sasaki et al., 2006). The hindcast begins from the result of a previous OFES hindcast simulation forced by NCEP/NCAR reanalysis from 1950 (Sasaki et al., 2008).

A sensitivity simulation from July 1999 to 2008 was conducted using the OFES to observe how the HLCC varied interannually, without interannual variations of local wind forcing near Hawaii. The simulation is forced by the same forcings as the hindcast simulation, but the wind stress in the region around Hawaii (170°W−155°W, 15°N−23°N) is replaced by the climatological mean fields averaged from 2001 to 2008. In a buffer zone with a width of 2° outside the region, the wind stress is gradually tapered to the interannually varying field, reducing the discontinuity at the boundary of the region.

3. Interannual variations in observations

3.1 HLCC and trade winds

Figure 1a shows the long-term mean eastward speed of the geostrophic current estimated from the AVISO SSH averaged from 2001 to 2008. A narrow eastward current along approximately 19.5°N, corresponding to the HLCC, extends westward from Hawaii across the dateline. The HLCC path tilts slightly southward toward the west. The current speed averaged between 180° and 160°W along 19.5°N is 6.8 cm s^{-1}, which is comparable to the value of 6.3 cm s^{-1} estimated from historical hydrographic data (Kobashi and Kawamura 2002).

The annual mean HLCCs in 2003 and 2005 were markedly stronger west of 170°W compared with the multi-year average from 2001 to 2008 (Fig. 1). Sasaki et al. (2010) found the HLCC accelerations away from Hawaii and suggested that the wind-driven mechanism is not dominant in these accelerations. Here, we examine separately the interannual variations of the HLCC near (between 165°W and 160°W) and away from (between 180° and 165°W) Hawaii.

Time-latitude plots of 13 month running means of the eastward current speed averaged between 180° and 165°W exhibit distinct interannual variations of the HLCC, capturing the events of HLCC enhancement away from Hawaii that occurred in both 2003 and 2005 (Fig. 2a). If the HLCC accelerations can be explained by the wind-driven mechanism through trade wind variations, the winds and orographic wind curl dipole must be strong during the same periods. The meridional gradient of the wind stress curl dipole must also be large based on the Sverdrup theory for estimating mass transport. However, Figure 3 shows that the easterly wind and meridional gradient of the wind stress curl in the lee of the Hawaii were not strong in 2003 and 2005. The discrepancies between the variations of the HLCC and those of the trade winds with the wind curl dipole suggest that the HLCC accelerations are mainly induced by other mechanisms that are not associated with trade wind variability.

Near Hawaii, the HLCC was strong not only in 2003 and 2005 but also in 2001 and 2007 (Fig. 2b). The HLCC accelerations in 2003 and 2005 are similar to but weaker than those away from Hawaii (Fig. 2a), and, as discussed above, are not due to the wind-driven mechanism. However, the wind-driven mechanism associated with the strong trade winds in 2001 and 2007 (Fig. 3) seems to have accelerated the HLCC near Hawaii (Fig. 2b). The HLCC was weak in 2004 both near (Fig. 2b) and farther from Hawaii (Fig. 2a) compared with the previous and subsequent years. It is possible that the anomalous weak trade winds in 2004 induced HLCC deceleration not only near Hawaii but also farther from Hawaii by the wind-driven mechanism. These results suggest some influence of the wind-driven mechanism on interannual variations of the HLCC both near Hawaii and farther from Hawaii, although this mechanism is not the main factor in the HLCC accelerations away from Hawaii in 2003 and 2005.

The Argo observations from the MOAA GPV dataset also feature the mean HLCC (not shown) and the accelerations away from Hawaii in 2003 and 2005 (Fig. 2c). However, there are some differences from the altimeter observations. Compared to the altimeter observations (Figs. 1a and 2a, b), the mean HLCC is relatively broad and its speed is about half (not shown). In addition, the magnitude of the interannual variations is much smaller (Fig. 2c, d). These discrepancies are possibly because of sparse observations and smoothing of the dataset by the OI method. The Argo observations display another peak of the high speed away from Hawaii in 2007 (Fig. 2c), which could be contaminated by the strong HLCC near Hawaii forced by the strong wind (Figs. 2b and 3).

3.2 Subsurface PV

Argo observations capture the interannual accelerations in 2003 and 2005 (Fig. 2c), which encourages us to examine subsurface PV and its relationship to the HLCC variations. Figure 4 shows a latitude–depth section for PV and potential density averaged between 180° and 165°W away from Hawaii. In the multi-year mean plot (Fig. 4a), the pycnocline around 24.2 σ_θ slopes up northward most steeply between 18°N and 21°N. A surface-intensified eastward current corresponding to the HLCC is consistently positioned at the latitudes of the steep pycnocline slope.

The annual mean main pycnocline slope in 2005 was steeper around 20°N than the multi-year mean from 2001 to 2008 (Fig. 4c), which is consistent with the highest HLCC speed away from Hawaii in that year based on the Argo dynamic height (Fig. 2c). We found negative PV anomalies in the density range of 24.6−25.8 σ_θ north of 18°N in 2005 (Fig. 4c). If the HLCC intensification was induced by the wind-driven mechanism, the PV anomalies would be localized near the HLCC in the meridional direction by Rossby wave propagations, but they actually extend north across 30°N. Therefore, the PV anomalies are likely to have been induced by some other mechanism and appear to have accelerated the HLCC based on the mechanism proposed by Kubokawa (1999);

however, Kobashi et al. (2006) suggested that the climatological HLCC front east of the dateline is not induced by low PV mode water intrusions. In 2003 (Fig. 4b), negative PV anomalies spread further southward than those in 2005, extending south across 20°N at the depth of 100−200 m. The pronounced negative anomalies north of the HLCC push isopycnals upward along the southern flank of the PV anomalies, intensifying the eastward HLCC. These results suggest that the negative PV anomalies north of the HLCC may contribute to interannual variations of HLCC speed.

We examine the horizontal distribution of PV anomalies. The long-term mean PV at 25.0 σ_θ in the Argo observations (Fig. 5a) captures the Eastern Subtropical Mode Water (ESTMW; Hautala and Roemmich, 1998). The ESTMW is characterized by a subsurface low PV water mass with a density range of 24.0–25.4 σ_θ, which is distributed east of Hawaii in the eastern subtropical North Pacific. The STMW is another low PV water mass with lowest PV at 25.4–25.5 σ_θ. The long-term mean PV at 25.4 σ_θ (Fig. 5b) shows that the STMW is located in the northwestern subtropical gyre (e.g. Suga and Hanawa, 1995; Kobashi et al., 2006). The formations of the ESTMW (Toyoda et al., 2011) and STMW (e.g., Suga and Hanawa, 1995; Oka, 2009) display considerable interannual variations.

Interannual variations of the isopycnal PV were examined to investigate the relationship with the HLCC variations. We observed isopycnal PV variations south of the southernmost outcrop line of the isopycnal surface among the lines from 2001 to 2008, because interannual variations of the outcrop line are not discussed here. In 2003, PV anomalies were negative to the north of the HLCC at 20°N (Fig. 6a and 6c). To determine how the anomalies extended north of the HLCC, we plotted PV anomalies along a long-term mean acceleration potential isoline (Fig. 7). The horizontal gradient of the acceleration potential corresponds approximately to the geostrophic current on an isopycnal surface (Montgomery and Stroup, 1962). Although the acceleration potential isolines varied interannually in the zonal direction approximately 5° east of Hawaii at approximately 25°N (not shown), the PV variability can be roughly traced along the mean isoline. At the 25.0 σ_θ surface, the negative anomalies between 170°W and 160°W from 2003 to early 2004 can be traced back to approximately 150°W from late 2002 to early 2003 (Fig. 7a), suggesting a southwestward intrusion of low PV water from the western edge of the ESTMW. The PV anomalies enhanced the meridional negative PV gradients to the south of the anomalies. At the 25.4 σ_θ surface, the negative PV anomalies were distributed between 175°W and 155°W west of Hawaii in 2003 but do not extended further east (Fig. 6c). These negative PV anomalies cannot be traced back clearly along the acceleration potential isoline (Fig. 7b).

In 2005, negative PV anomalies were distributed west of Hawaii and north of 18°N at the 25.0 and 25.4 σ_θ surfaces (Figs. 6b and 6d). The negative anomalies at the 25.0 σ_θ surface between 180° and 170°W in late 2005 appear to have migrated westward from the east (Fig. 7a). At the 25.4 σ_θ surface (Fig. 7b), the negative anomalies at approximately 170°W in 2005 appear to have been induced by an eastward expansion of the STMW to approximately 160°W in the same period (Fig. 6d). These negative PV anomalies at the 25.0 and 25.4 σ_θ surfaces both enhanced meridional PV gradients to the south of the PV anomalies (Fig. 7).

From late 2004 to early 2005, the negative PV anomalies at both the 25.0 σ_θ and the 25.4 σ_θ surfaces were relatively weak at approximately 170°W−160°W near Hawaii compared to before and after this period (Fig. 7). The anomalously weak trade winds and meridional gradient of the wind curl near Hawaii in this period (Fig. 3) likely reduced the pycnocline slanting along the HLCC by the wind-driven mechanism via Rossby waves and then weakened the negative PV anomalies and their meridional gradients near Hawaii. After passing the Rossby waves, the pycnocline slanting along the HLCC could get back to the former state. We also found positive PV anomalies to the south of the HLCC at the 25.4 σ_θ surface in 2003 and at the 25.0 σ_θ and 25.4 σ_θ surfaces in 2005 (Fig. 6). This result suggests that not only PV anomalies north of the HLCC but also PV anomalies to the south and a wind forcing around Hawaii influence interannual variations of the HLCC.

3.3 Contributions of subsurface PV variability to the HLCC

The eastward countercurrent is associated with a slanting pycnocline based on the thermal wind balance theory. This section examines the contributions of PV anomalies to the pycnocline slope following the method of Kobashi et al. (2006), who showed that the STFs and STCCs are anchored by large negative PV gradients. Under the assumption that relative vorticity is negligible, PV (q) is defined in a vertical coordinate system of density ρ by

$$q(\rho)=-\frac{f}{\rho_0 \partial Z(\rho)/\partial \rho} \quad (1),$$

where Z is the depth of the isopycnal surface and is negative below sea level, f is the planetary vorticity, and ρ_0 is the reference density. Solving Z and taking the meridional derivative, the isopycnal slope is estimated by

$$\left(\frac{\partial Z(\rho)}{\partial y}\right)_\rho=-\frac{1}{\rho_0}\int_{\rho_b}^{\rho}\frac{1}{q(\rho')}\left(\beta-\frac{f}{q(\rho')}\left(\frac{\partial q(\rho')}{\partial y}\right)_\rho\right)d\rho'+\left(\frac{\partial Z_0(\rho_b)}{\partial y}\right)_\rho \quad (2),$$

which is identical to Equation (3) in Kobashi et al. (2006). Here, Z_0 is the depth of the reference isopycnal surface ρ_b ($\geq \rho$), and β is the meridional gradient of f. The subscript ρ denotes a partial derivative on a constant density surface. For the isopycnal surface of density ρ to slope up toward the north, the PV gradient deviation (β-(f/q)($\partial q/\partial y$)$_\rho$) should be a large positive value above the reference isopycnal surface.

Figure 8 shows the meridional section of PV, meridional PV gradients, and meridional density gradients averaged between 180° and 165°W. The mean plot (Fig. 8a) averaged from 2001 to 2008 is similar to the hydrographic observations (Fig. 7c in Kobashi et al., 2006). Large negative PV gradients ($< -2.0\times10^{-11}$ m^{-1}s^{-1}) in the density range of 24.6–25.7 σ_θ are distributed below the strong density front ($> 15\times10^{-7}$ kg m^{-4}) at approximately 20°N, corresponding to the HLCC. The negative PV gradients in the density range lighter than 25.0 σ_θ are distributed south of the latitude of HLCC. No local minimum PV corresponding to the mode water is found north of the front, consistent with results of by Kobashi et al. (2006). The large negative PV gradients are probably induced by a pycnocline slanting along the HLCC through Rossby waves under the wind-driven mechanism.

Large negative PV anomalies north of the HLCC seem to have accelerated the current in 2003 and 2005, as suggested in Section 3.2. To test this hypothesis, we examined the contributions of PV anomalies to HLCC acceleration based on Equation (2). The negative PV gradients were larger ($< -2.0\times10^{-11}$ m^{-1}s^{-1}) in the density range around 25.2 σ_θ (25.0 σ_θ) at the latitude of the HLCC in 2003 (2005) than those averaged from 2001 to 2008 (Fig. 8). Above the negative PV gradients, large meridional density gradients (> 2.0×10^{-6} kg m^{-4}) were found at densities less than 23.8 σ_θ (24.2 σ_θ) in 2003 (2005) at approximately 19°N, leading to a strong eastward HLCC. Figure 9 shows a comparison of profiles of minimum PV gradients between 18°N and 21°N around the latitude of the HLCC. The negative PV gradients in both 2003 and 2005 were larger in the density range of 24.3–25.5 σ_θ compared to the mean values from 2001 to 2008. These results confirm that large negative PV anomalies north of the HLCC accelerate the HLCC in 2003 and 2005.

We compared the time series of the vertical integration of the meridional PV gradient from the 24.5 σ_θ to 25.5 σ_θ surfaces and the meridional slope of the 24.2σ_θ isopycnal (Fig. 10) in order to observe contributions of interannual variations of PV anomalies north of the HLCC on the HLCC variations in detail. The slope is linked to the HLCC speed by the thermal wind relationship and was steeper in 2003, 2005 and 2007 than in other years. Although the standard deviation of the 13 month running mean of the pycnocline slope (1.54×10^{-5} m/m) is about double of that of the PV gradient integration (0.86×10^{-5} m/m), the high correlation between the time series suggests that the PV gradient contributed to the isopycnal slope variations. However, the contribution seems to have been small in 2007. The strong trade winds in that year (Fig. 3) may have caused the isopycnal to slope upward locally along the HLCC through the wind-driven mechanism. The results suggest that the HLCC is mainly enhanced by low PV water intrusions to its north, but the wind-driven mechanism associated with trade wind variations may also influence interannual variations of the HLCC.

4. Mechanism of interannual HLCC variations in the OGCM

4.1 Interannual variations in the hindcast simulation

Sasaki et al. (2010) described interannual variations of HLCC speed based on the OFES hindcast simulation driven by daily mean QuikSCAT wind stress. Figure 2e shows that the HLCC away from Hawaii was relatively strong from mid 2001 to late 2006, with two peaks in 2003 and 2005 in the hindcast simulation as seen in Sasaki et al. (2010). Near Hawaii, the simulated HLCC was strong not only in 2003 and 2005 but also in 2001 and 2007 (Fig. 2f). The accelerations in 2001 and 2007 and the deceleration in 2004 seem to be due to the wind-driven mechanism, as seen in Section 3.

There are some discrepancies between the interannual variations of the HLCC seen in the hindcast simulation and those in satellite observations. The durations of the HLCC accelerations in the simulations (Fig. 2e) are different by several months from those seen in the observational data (Fig. 2a), although the periods with the peaks of HLCC speed in 2003 and 2005 almost overlap with those in the observations. The HLCC acceleration in 2005 was relatively weak in the simulation (Fig. 2e), whereas near Hawaii, the HLCC accelerations in 2003 and 2007 were stronger (Fig. 2f) than those in the observations (Fig. 2b). Several factors contribute to these disagreements. The wind forcing was switched from NCEP/NCAR reanalysis to QuikSCAT satellite observations in 1999, and it takes several years to adjust to this wind forcing change. Local eddy-mean flow interactions may also play a role (e.g., Kobashi and Kawamura, 2001). Regardless of these deficiencies, it is worth observing how low PV water induced interannual variations of the HLCC from 2001 to 2008 in the simulation that provides an oceanic field dynamically consistent with the primitive equations of the OGCM, because the Argo grid data are smoothed by the OI method, and error ratio of the grid data is large before 2002 due to sparse observations (Hosoda et al., 2008).

The OFES hindcast simulation reproduces observed mean PV distribution on isopycnal surfaces well (Fig. 11), although the center of the STMW at the 25.4 σ_θ surface is shifted eastward by approximately 5°, and the PVs become too large eastward in the eastern Pacific at both the 25.0 σ_θ and the 25.4σ_θ surfaces compared with the Argo observations (Fig. 5). Figure 12 shows that negative PV anomalies north of the HLCC at the 25.0 σ_θ (25.4 σ_θ) surface in 2003 (2005) spread eastward across Hawaii (between 170°E and Hawaii). Both negative PV anomalies can be traced back to just south of the winter outcrop line along the mean acceleration potential isolines (Fig. 13a and 13b). The paths of the PV anomalies seem clearer than those in Argo observations (Fig. 7), probably because of the scarce observations and the smoothing of the dataset by the OI method. These results suggest influences of ESTWM (STMW) variations in 2003 (2005) on the HLCC accelerations, similar to what is seen in Argo observations.

In 2004, the negative PV anomalies between 180° and 170°W were small, and the meridional gradient anomalies south of the acceleration potential isoline were positive at the 25.0 σ_θ surface (Fig. 13a). The weak negative PV anomalies seem to have been caused by weakening of the pycnocline slope localized along the HLCC that is probably due to the wind-driven mechanism through Rossby waves associated with anomalously weak trade winds in 2004 (Fig. 3). In 2006, the negative PV anomalies were large between 180° and 160°W at the 25.4 σ_θ surface (Fig. 13b), but the meridional PV gradient anomalies were mostly positive because of negative PV anomalies spreading to the south of the HLCC (not shown). In addition to low PV intrusions north of the HLCC, the wind-driven mechanism and the low PV south of the HLCC may influence interannual variations of the HLCC in the simulation, as evaluated using the observations presented in Section 3.

4.2 Sensitivity simulation without interannual wind variations around Hawaii

A sensitivity experiment that dose not include interannual wind variations around Hawaii was conducted to determine whether the wind-driven mechanism or other mechanisms, including low PV water intrusions, cause the interannual variations of the HLCC. If the HLCC variations away from Hawaii were similar between the sensitivity and hindcast simulations, the wind-driven mechanism could be excluded as a mechanism causing HLCC variations. The sensitivity simulation (Fig. 2g) captures the HLCC acceleration away from Hawaii in 2003 similarly to the hindcast simulation (Fig. 2e), suggesting that the HLCC acceleration was not caused by the wind-driven mechanism. At the 25.0 σ_θ surface, negative PV anomalies between 175°W and 160°W, which migrated from east-northeast in 2003 (Fig. 13c), seem to have caused negative meridional PV gradients and pushed up the pycnocline above the PV anomalies, accelerating the HLCC.

However, the acceleration of the HLCC in 2005 was less clear in the sensitivity simulation (Fig. 2g). The negative PV anomalies migrated along the acceleration potential isoline at the 25.4 σ_θ surface (Fig. 13d), but they were weaker between 180° and 160°W in 2005 than those in the hindcast simulation (Fig. 13b). The weak negative PV anomalies did not result in large meridional PV gradient along the HLCC (Fig. 13d). The spreading of low PV water to the south of the HLCC in that year also seems to have weakened the negative PV gradient (not shown).

The interannual variations of the HLCC near Hawaii are weakened in the sensitivity simulation but do not disappear completely (Fig. 2h). The remaining HLCC variations could arise from mechanisms other than wind-driven mechanism, including low PV water intrusions and wind variability east of Hawaii via Rossby wave propagations. In contrast, the acceleration (deceleration) in 2007 (2004) dose not occur in the sensitivity simulation, supporting that these variations are induced by a wind curl forcing around Hawaii. The acceleration in 2001, which is also suggested to result from a wind-driven mechanism as well as in 2007, still remains, but weakens compared to before and after the year. These results suggest that interannual variations of the HLCC near Hawaii are partially induced by the wind-driven mechanism.

5. Discussion

This section discusses formation mechanism of the low PV anomalies that influence on interannual variations of the HLCC. Our analyses suggest that variations of the ESTMW (STMW) could contribute to low PV water intrusions north of the HLCC in 2003 (2005). In the Argo observations (Fig. 7a) and the OFES hindcast simulation (Fig. 13a), negative PV anomalies at the 25.0 σ_θ surface north of the HLCC accelerating the current in 2003 can be traced back to the western edge of the ESTMW in 2002. The anomalously deep mixed layer in the western portion of the ESTMW in 2002 (not shown) could enhance ESTMW formation. Toyoda et al. (2011) studied the interannual variability of ESTMW formation in the 1990s and suggested that winter atmospheric cooling, Ekman convergence of salty water, and insolation change due to low-level cloud cover are important in this process. Detailed analyses of ESTMW interannual variations in the 2000s are beyond the scope of our study.

In the hindcast simulation, the negative PV anomalies at the 25.4 σ_θ surface north of the HLCC in 2005 can be traced back to the northeastern edge of the STMW in 2003 (Fig. 13b). The HLCC acceleration in 2005 was relatively weak in the simulation compared with the Argo observations (Fig. 2). However, it is worth discussing the interannual variations of STMW formation in the simulated oceanic field, since dynamical interpretation is available using outputs from the OGCM. The simulated mixed layer in the STMW formation region was anomalously deep in 2003 in the winter (Fig. 14), consistent with historical observations (Qiu and Chen, 2006; Sugimoto and Hanawa, 2010). Previous studies have suggested that wind variations (Suga and Hanawa, 1995), stability of the Kuroshio Extension path (Qiu and Chen, 2006), and the meridional migration of the Aleutian Low (Sugimoto and Hanawa, 2010) lead to interannual variations in mixed layer depth and STMW formation. We found anomalously strong westerly wind stress in the region of the anomalously deep mixed layer in 2003 in the winter (Fig. 14). The northwest monsoon was anomalously strong during this winter, probably due to a strong Aleutian low, based on the North Pacific Index (NPI, Trenberth and Hurrell, 1994). It appears that strong westerly winds cause a deeper mixed layer via strong surface cooling that intensifies STMW formation. The subsequent southward intrusion of low PV water from the northeastern edge of the STMW enhanced the HLCC in 2005 in the hindcast simulation. This mechanism is consistent with findings from previous studies on decadal changes in the STCC by Yamanaka et al. (2008) using an OGCM and Xie et al. (2011) using a coupled GCM.

In the ocean hindcast simulation forced by observed wind variability, mode waters display considerable decadal variability, especially in OGCMs of moderate resolution (~1^{o}) (Xie et al. 2000; Hosoda et al. 2004). In an eddy-resolving simulation, such mode-water variability has been found to induce significant changes in STCC (Yamanaka et al. 2008). Nonaka et al. (2011, this issue) examined this mode-water effect on the interannual variability of STCC in a hindcast simulation using the OFES forced by NCEP/NCAR reanalysis. In coupled ocean-atmosphere simulations, mode water changes are the dominant mechanism for STCC variability, with obvious effects on the atmosphere due to thermal advection by anomalous surface currents (Xie et al. 2011). Accumulation of Argo observations will enable critical examination of this mode water-induced mechanism for surface current variability, including its relationship to STCCs and the HLCC.

It appears that low PV water is important for interannual variations of the HLCC in the 2000s. Other mechanisms, including the wind-driven mechanism, might cause HLCC acceleration on interannual to decadal time scales. The Pacific Decadal Oscillation (PDO; Mantua et al., 1997) could induce HLCC variation. Variations of mixed layer depth (Carton et al. 2008) and low PV water subduction (Qu and Chen, 2009; Chen et al., 2010) associated with the PDO may influence the HLCC via variations of pycnocline slope. Mean-flow acceleration through eddies (Kobashi and Kawamura, 2001, Liu and Li, 2007) may also play a role. As the present study covers a short period of time, it does not rule out a role for the wind-driven mechanism in HLCC variability, which is considerable near Hawaii. In the OFES hindcast simulation forced by the NCEP/NCAR reanalysis for 1950–2008, the wind-driven mechanism is dominant in the interannual and decadal variability in the HLCC (not shown). However, the simulation does not capture the HLCC accelerations in 2003 and 2005 (not shown). The orographic wind stress curl dipole west of Hawaii in the reanalysis is too strong, and its distributions are too broad.

It is possible that air-sea interactions accompanied by the HLCC with high SST (Xie et al., 2001) play a role in interannual variations of the HLCC. In 2003 and 2005, an elongated positive wind stress curl extended westward from Hawaii at approximately 19°N, tilting slightly southward in a more distinct manner than in other years based on QuikSCAT observations (not shown). In both years, the HLCC based on the AVISO observations was strong, and its position almost overlapped that of the positive wind stress curl, suggesting that the distinct curl away from Hawaii could further enhance the strong HLCC. These results suggest that acceleration of the HLCC due to local air-sea interactions (Sasaki and Nonaka, 2006) could further amplify the interannual variations of the HLCC.

6. Conclusions

We investigated the interannual variations of the HLCC in the 2000s using satellite and Argo observations and high-resolution OGCM simulations. The current speed was high in 2003 and 2005, when the trade winds and the orographic wind stress curl dipole in the lee of Hawaii were not particularly strong. Furthermore, the HLCC acceleration took place more strongly away from Hawaii. The results suggest that the wind-driven mechanism is not the leading factor causing the HLCC accelerations in these two years. Subsurface PV variations appear to be important in these accelerations. We found that negative PV anomalies in subsurface layers, which were advected to the north of the HLCC, pushed the upper pycnocline upward and enhanced the eastward HLCC through the thermal wind relation, following the mechanism proposed by Kubokawa (1999). The OFES sensitivity simulation forced by wind stress that does not include the interannual variability near Hawaii confirms that the HLCC acceleration away from Hawaii in 2003 was not induced by the wind-driven mechanism. In addition to low PV anomalies, the wind-driven mechanism is also suggested to be important in variations of the HLCC near Hawaii.

We examined the causes of interannual variations in low PV water intrusions. Subsurface low PV anomalies can be traced back to the winter outcrop line, especially in the simulations. ESTMW and STMW intrusions appear to have driven the HLCC accelerations in 2003 and 2005, respectively, although the HLCC is located away from the cores of these mode waters. Detailed analyses will be needed as Argo observations accumulate in the future. The atmospheric variations responsible for HLCC interannual to decadal variations via water mass subduction also remain to be investigated.

Acknowledgments

The OFES simulations were conducted on the Earth Simulator under support from JAMSTEC. We thank Drs. B. Qiu and F. Kobashi for valuable discussions and the reviewers for valuable comments. We thank T. Ohira for his help in constructing the MOAA GPV product. QuikSCAT wind stress data in the J-OFURO dataset were provided by Dr. K. Kutsuwada. This study was supported in part through Grant-In-Aid for Scientific Research 22106006 and that on Innovative Areas #2205 by the Japanese Ministry of Education, Culture, Sports, Science and Technology, and also through 23340139 by the Japan Society for the Promotion of Science. IPRC/SOEST publication ###/####.

References

Aoki, Y., T. Suga and K. Hanawa (2002), Subsurface subtropical fronts of the North Pacific as inherent boundaries in the ventilated thermocline, *J. Phys. Oceanogr.*, 32, 2299–2311.

Bingham, F. (1992), The formation and spreading of subtropical mode water in the North Pacific, *J. Geophys. Res.*, 97, 11177–11189.

Boyer, T. P., C. Stephens, J. I. Antonov, M. E. Conkright, R. A. Locarnini, T. D. O'Brien, and H. E. Garcia (2002), World Ocean Atlas 2001, vol. 2: Salinity, NOAA Atlas NESDIS 50, U.S. Gov. Print. Off.,Washington, D. C., 165pp.

Carton, L., S. A. Grodsky, and H. Liu (2008), Variability of the oceanic mixed layer, 1960-2004, *J. Climate*, 21, 1029–1047.

Chen, J., T. Qu, Y. N. Sasaki, and N. Schneider (2010), Anti-correlated variability in subduction rate of the western and eastern North Pacific Oceans identified by an eddy-resolving ocean GCM, *Geophys. Res. Lett*., 37, L23608, doi:10.1029/2010GL045239.

Flament, P., S. Kennan, R. Lumpkin, M. Sawyer, and E. Stroup (1998), The ocean, in *Atlas of Hawaii*, edited by S. P. Juvik and J. O. Juvik, pp. 82–86, Univ. of Hawaii Press, Honolulu.

Hafner, J., and S.-P. Xie (2003), Far-field simulation of the Hawaiian wake: sea surface temperature and orographic effects, *J. Atmos. Sci.*, 60, 3021–3032.

Hanawa, K. and L. D. Talley (2001), Mode waters, in *Ocean Circulation and Climate*, ed. By J. Church et al., pp. 373–386, Academic Press, London.

Hautala, S., and D. Roemmich (1998), Subtropical mode water in the Northeast Pacific Basin, *J. Geophys. Res*., 103(C6), 13055-13066.

Hosoda, S., S.-P. Xie, K. Takeuchi and M. Nonaka (2004), Interdecadal temperature variations in the North Pacific central mode water simulated by an OGCM. *J. Oceanogr.*, 60, 865-877.

Hosoda, S., T. Ohira, and T. Nakamura (2008), A monthly mean dataset of global oceanic temperature and salinity derived from Argo float observations, *JAMSTECR*, 8, 47–59.

Kalnay, E., M. Kanamitsu, R. Kistler, W. Collins, D. Deaven, L. Gandin, M. Iredell, S. Saha, G. White, J. Woollen, Y. Zhu, M. Chelliah, W. Ebisuzaki, W. Higgins, J. Janowiak, K.C. Mo, C. Ropelewski, A. Leetmaa, R. Reynolds, and R. Jenne (1996), The NCEP/NCAR 40-year reanalysis project, *Bull. Amer. Meteor. Soc.*, 77, 437–471.

Kobashi, F., and H. Kawamura (2001), Variation of sea surface height at periods of 65-220 days in the subtropical gyre of the North Pacific, *J. Geophys. Res.*, 106, 26817–26831.

Kobashi, F., and H. Kawamura (2002), Seasonal variation and instability nature of the North Pacific Subtropical Countercurrent and the Hawaiian Lee Countercurrent, *J. Geophys. Res.*, 107, 3185, doi:10.1029/2001JC001225.

Kobashi, F., H. Mitsudera, and S.-P. Xie (2006), Three subtropical fronts in the North Pacific: Observational evidence for mode water-induced subsurface frontogenesis, *J. Geophys. Res.*, 111, C09033, doi:10.1029/2006JC003479.

Kubokawa, A. (1999), Ventilated thermocline strongly affected by a deep mixed layer: A theory for subtropical countercurrent, *J. Phys. Oceanogr.*, 29, 1314–1333.

Kubokawa, A., and T. Inui (1999), Subtropical countercurrent in an idealized ocean GCM, *J. Phys. Oceanogr.*, 29, 1303–1313.

Kubota, M., N. Iwasaka, S. Kizu, M. Konda, and K. Kutsuwada (2002), Japanese ocean flux data sets with use of remote sensing observations (J-OFURO), *J. Oceanogr.*, 58, 213-225.

Kutsuwada, K. (1998), Impact of wind/wind-stress field in the North Pacific constructed by ADEOS/ NSCAT data, *J. Oceanogr.*, 54, 443–456.

Liu, Q. and L. Li (2007) Baroclinic stability of oceanic Rossby wave in the North Pacific Subtropical Countercurrent, *Chinese J. Geophys.*, 50 (1), 84–93.

Mantua, N. J., S. R. Hare, Y. Zhang, J. M. Wallace, and R. C. Francis (1997), A Pacific interdecadal climate oscillation with impacts on salmon production, *Bull. Amer. Meteor. Soc.*, 78, 1069-1079.

Masumoto, Y., H. Sasaki, T. Kagimoto, N. Komori, A. Ishida, Y. Sasai, T. Miyama, T. Motoi, H. Mitsudera, K. Takahashi, H. Sakuma, and T. Yamagata (2004), A fifty-year eddy-resolving simulation of the world ocean: preliminary outcomes of OFES (OGCM for the Earth Simulator), *J. Earth Simulator*, 1, 35–56.

Montgomery, R. B. and E. D. Stroup (1962), Equatorial waters and currents at 150°W in July–August 1952, *Johns Hopkins Oceanographic Studies*, 1, p. 68.

Nonaka, M., S.-P. Xie, and H. Sasaki (2011), Interannual variations in low potential vorticity water and the subtropical countercurrent in an eddy-resolving OGCM, *J. Oceanogra.*, doi:10.1007/s10872-011-0042-3.

Oka, E. (2009), Seasonal and interannual variation of North Pacific Subtropical Mode Water in 2003–2006, *J. Oceanogr.*, 65, 151–164, doi:10.1007/s10872-009-0015-y.

Pacanowski, R. C., and S. M. Griffies (1999), The MOM 3 Manual, GFDL Ocean Group Technical Report No. 4, Princeton, NJ: NOAA/Geophysical Fluid Dynamics Laboratory, 680 pp.

Qiu, B., D. A. Koh, C. Lumpkin, and P. Flament (1997), Existence and formation mechanism of the North Hawaiian Ridge Current, *J. Phys. Oceanogr.*, 27, 431–444.

Qiu, B. and S. Chen (2006), Decadal variability in the formation of the North Pacific Subtropical Mode Water: Oceanic versus atmospheric control, *J. Phys. Oceanogr.*, 36, 1365–1380, doi:10.1175/JPO2918.1.

Qu , T. and J. Chen (2009), A North Pacific decadal variability in subduction rate, *Geophys. Res. Lett.*, 36, L22602, doi:10.1029/2009GL040914.

Sakamoto, T. T., A. Sumi, S. Emori, T. Nishimura, H. Hasumi, T. Suzuki, and M. Kimoto (2004), Far-reaching effects of the Hawaiian Islands in the CCSR/NIES/FRCGC high-resolution climate model, *Geophys. Res. Lett.*, 31, L17212, doi:10.1029/2004GL020907.

Sasaki, H. and M. Nonaka (2006), Far-reaching Hawaiian Lee Countercurrent driven by wind-stress curl induced by warm SST band along the current, *Geophys. Res. Lett*., 33, L13602, doi:10.1029/2006GL026540.

Sasaki, H., Y. Sasai, M. Nonaka, Y. Masumoto, and S. Kawahara (2006), An eddy-resolving simulation of the quasi-global ocean driven by satellite-observed wind field: preliminary outcomes from physical and biological fields, *J. Earth Simulator*, 6, 35–49.

Sasaki, H., M. Nonaka, Y. Masumoto, Y. Sasai, H. Uehara, and H. Sakuma (2008), An eddy-resolving hindcast simulation of the quasi-global ocean from 1950 to 2003 on the Earth Simulator, in *High resolution numerical modelling of the atmosphere and ocean*, edited by W. Ohfuchi and K. Hamilton, Springer, New York, pp 157–186.

Sasaki, H., S.-P. Xie, B. Taguchi, M. Nonaka, and Y. Masumoto (2010), Seasonal variations of the Hawaiian Lee Countercurrent induced by the meridional migration of the Trade Winds, *Ocean Dynamics*, 60 (3), 705–715.

Smith, R. B. and V. Grubišic (1993), Aerial observation of Hawaii's wake, *J. Atmos. Sci.* 50, 3728–3750.

Stephens, C., J. I. Antonov, T. P. Boyer, M. E. Conkright, R. A. Locarnini, T. D. O'Brien, and H. E. Garcia (2002), World Ocean Atlas 2001, vol. 1: Temperature, NOAA Atlas NESDIS 49, U.S. Gov. Print. Off., Washington, D. C., 167 pp.

Suga, T., and K. Hanawa (1995), Interannual variations of North Pacific Subtropical Mode Water in the 137E section, *J. Phys. Oceanogr.*, 25, 1012–1017.

Sugimoto, S. and K. Hanawa (2010), Impact of Aleutian Low activity on the STMW formation in the Kuroshio recirculation gyre region, *Geophys. Res. Lett*., 37, L03606, doi:10.1029/2009GL041795.

Toyoda, T., T. Awaji, S. Masuda, N. Sugiura, H. Igarashi, T. Mochizuki, and Y. Ishikawa (2011), , Interannual variability of North Pacific eastern subtropical mode water formation in the 1990s derived from a 4-dimensional variational ocean data assimilation experiment. *Dyn. Atmos. Oceans*, 51(1-2), 1–25.

Trenberth, K. E. and J. W. Hurrell (1994), Decadal atmosphere-ocean variations in the Pacific, *Clim. Dyn.*, 9, 303-319.

Uda, M. and K. Hasunuma (1969), The eastward subtropical countercurrent in the western North Pacific Ocean, *J. Oceanogr. Soc. Jpn.*, 25, 201–210.

Xie, S.-P., T. Kunitani, A. Kubokawa, M. Nonaka and S. Hosoda (2000), Interdecadal thermocline variability in the North Pacific for 1958-1997: A GCM simulation. *J. Phys. Oceanogr.*, 30, 2798-2813.

Xie, S.-P., W. T. Liu, Q. Liu, and M. Nonaka (2001), Far-reaching effects of the Hawaiian Islands on the Pacific ocean-atmosphere system, *Science*, 292, 2057–2060.

Xie, S.-P., L.-X. Xu, Q. Liu, and F. Kobashi (2011), Dynamical role of mode-water ventilation in decadal variability in the central subtropical gyre of the North Pacific. *J. Climate*, *J. Climate*, 24, 1212–1225.

Yamanaka, G., H. Ishizaki, M. Hirabara, and I. Ishikawa (2008), Decadal variability of the Subtropical Front of the western North Pacific in an eddy-resolving ocean general circulation model, *J. Geophys. Res.*, 113, C12027, doi:10.1029/2008JC005002.

Yang, Y., S.-P. Xie, and J. Hafner (2008a), Cloud patterns lee of Hawaii Island: A synthesis of satellite observations and numerical simulation, *J. Geophys. Res.*, 113, D15126, doi:10.1029/2008JD009889.

Yang, Y., J. Ma, and S.-P. Xie (2008b), Observations of the trade wind wakes of Kauai and Oahu, *Geophys. Res. Lett*., 35, L04807, doi:10.1029/2007GL031742.

Yoshida, S., B. Qiu, and P. Hacker (2010), Wind-generated eddy characteristics in the lee of the island of Hawaii, *J. Geophys. Res.*, 115, C03019, doi:10.1029/2009JC005417.

Yu, Z., N. Maximenko, S.-P. Xie, and M. Nonaka (2003), On the termination of the Hawaiian Lee Countercurrent, *Geophys. Res. Lett.*, 30, 1215, doi: 10.1029/2002GL016710.

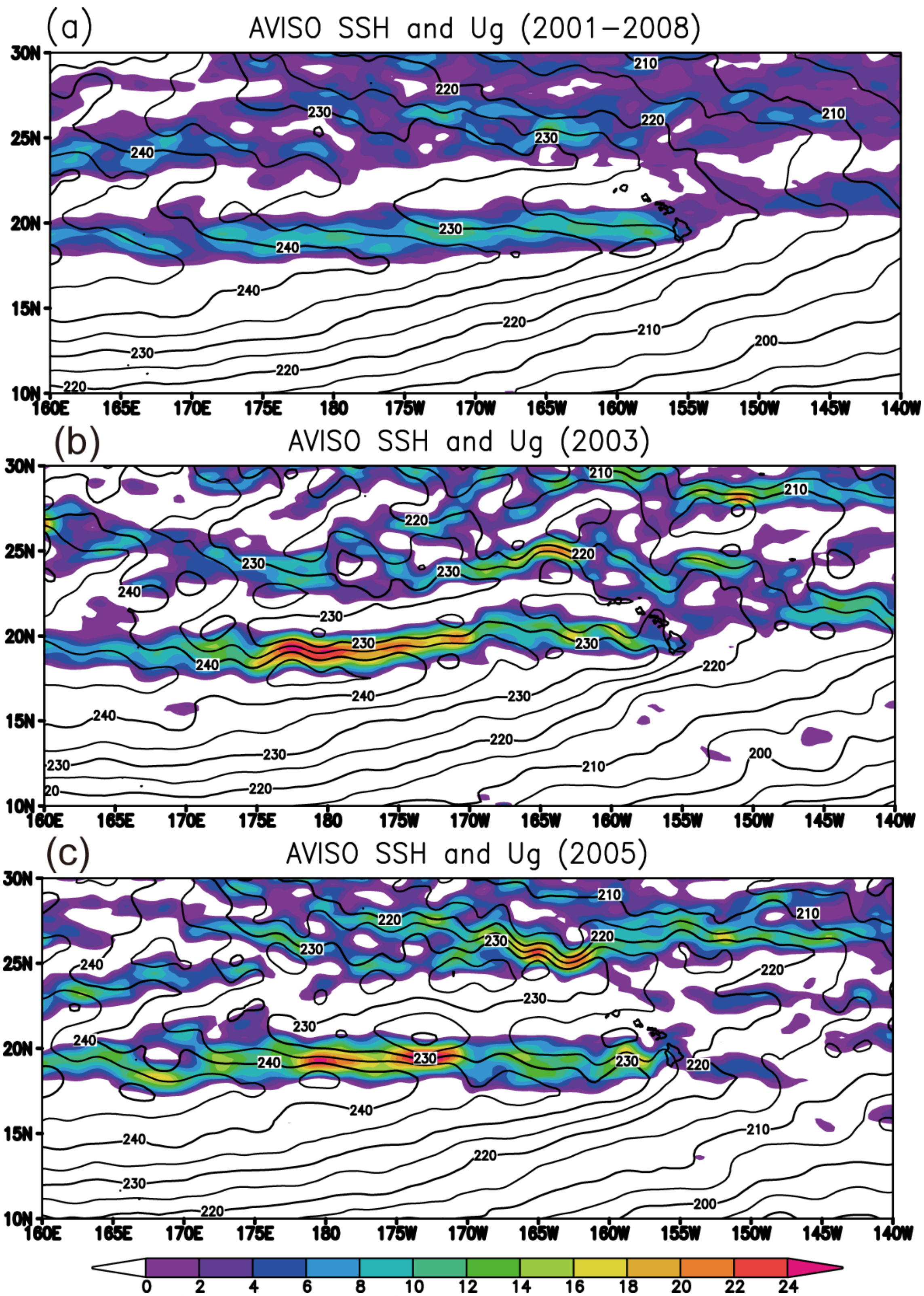

Figure 1. SSH (contour, unit is cm) and geostrophic eastward current speed

(color, unit is cm s^{-1}) based on the AVISO SSH. (a) Mean averaged from 2001 to 2008 and annual mean in (b) 2003 and (c) 2005.

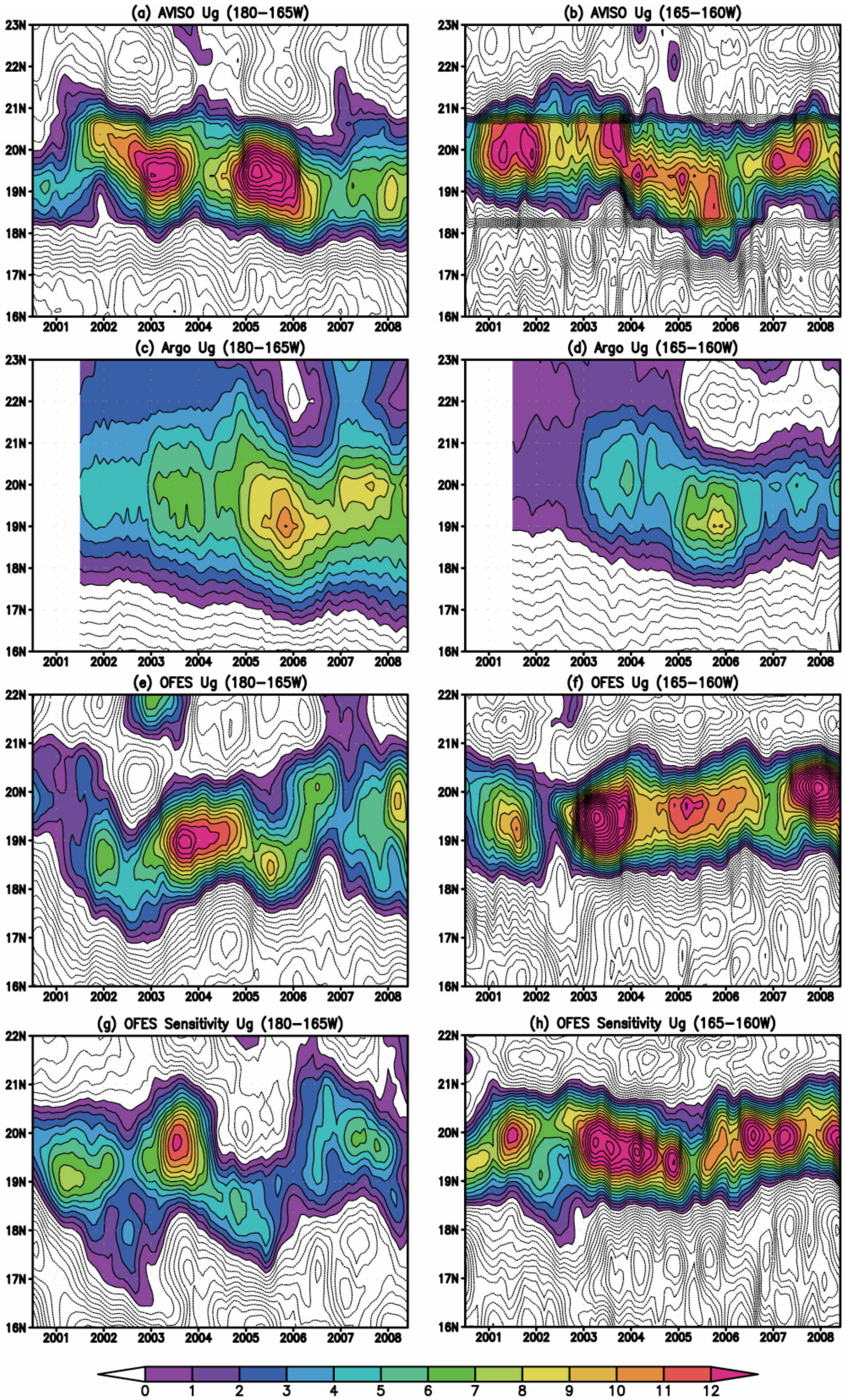

Figure 2. Time-latitude plots of 13 month running mean of the geostrophic eastward current (cm s^{-1}) averaged between (a, c, e, g) 180° and 165°W and (b,

d, f, h) 165°W and 160°W based on (a, b) the Aviso SSH, (c, d) dynamic height at 10 dbar referenced to 2,000 dbar of the MOAA GPV, (e, f) SSH of the OFES hindcast simulation, and (g, h) SSH of the OFES sensitivity experiment.

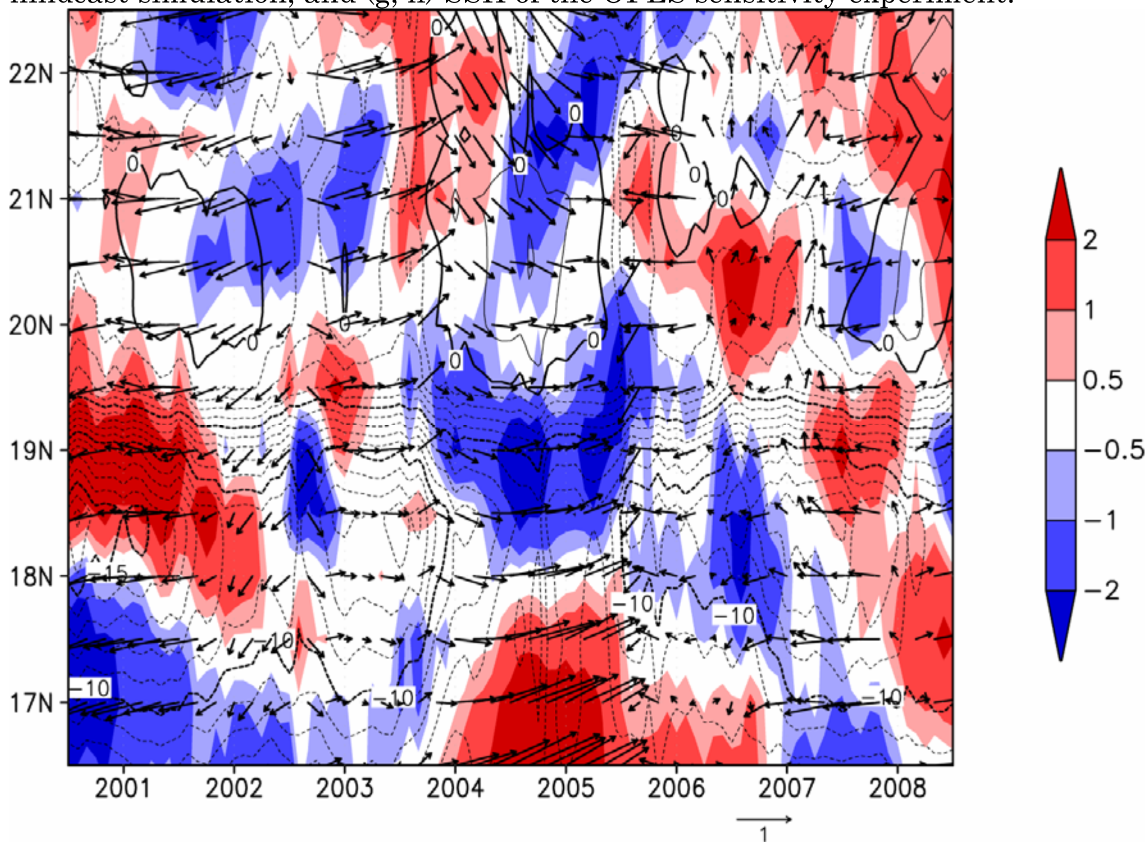

Figure 3. Anomalies of wind stress vectors (10^{-2} N m^{-2}) and meridional gradient of wind stress curl (color, unit is 10^{-13} N m^{-4}) averaged between 165°W and 157°W from the mean averaged from 2001 to 2008 based on QuikSCAT satellite observations. Contour indicates wind stress curl (10^{-8} N m^{-3}) averaged between 165°W and 157°W and its interval is 10^{-8} N m^{-3}. All variables are 13-month running mean values.

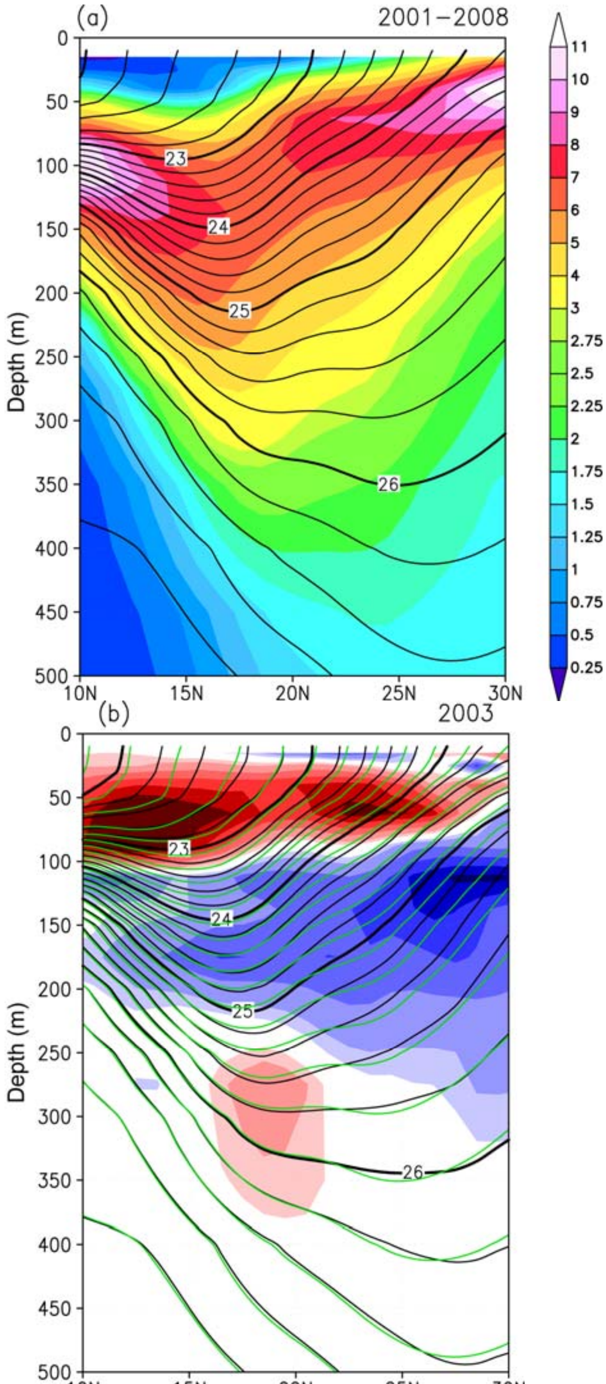

(a)
2001−2008
(b)
2003
Depth (m)
10N
15N
20N
25N
30N
23
24
25
26
11
10
9
8
7
6
5
4
3
2.75
2.5
2.25
2
1.75
1.5
1.25
1
0.75
0.5
0.25

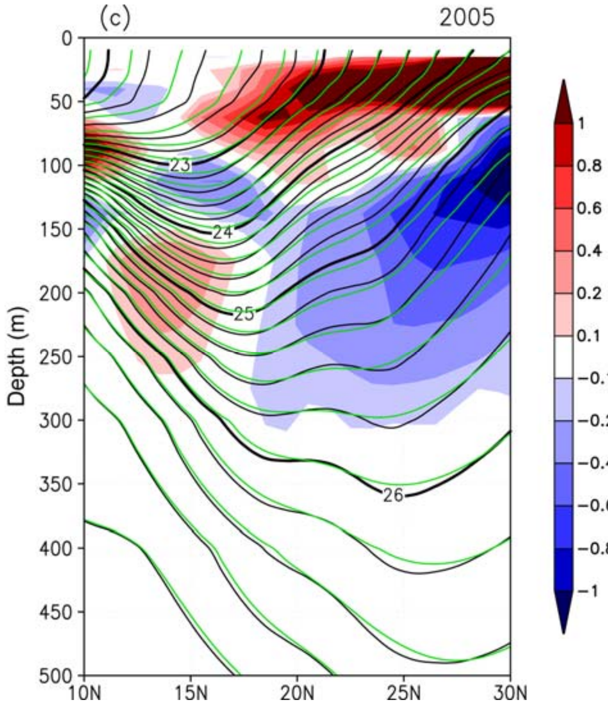

Figure 4. Latitude−depth section of PV (color: unit is 10^{-10} $m^{-1}s^{-1}$) averaged between 180° and 165° W based on the MOAA GPV. (a) Mean averaged from 2001 to 2008 and yearly anomalies from the mean in (b) 2003 and (c) 2005. Black contours indicate potential density (σ_θ) and their intervals are 0.2 σ_θ. Green contours in Fig. 4b and 4c indicate mean potential density averaged from 2001 to 2008.

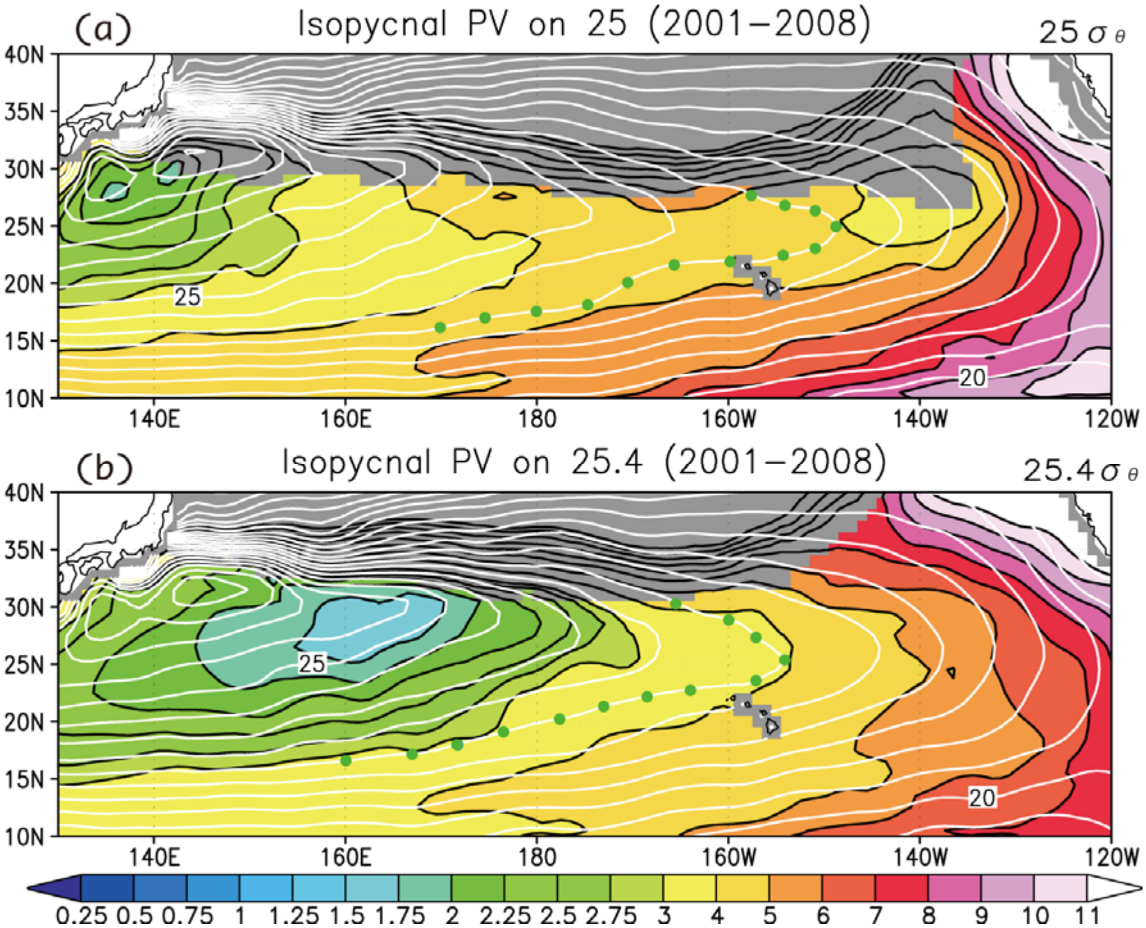

Figure 5. Mean PV (10^{-10} m^{-1}s^{-1}) averaged from 2001 to 2008 at the (a) 25.0 σ_θ and (b) 25.4 σ_θ surfaces based on the MOAA GPV. White contours indicate acceleration potential (m^2 s^{-2}) at 10 dbar relative to 2000 dbar. Contour interval is 0.5 m^2 s^{-2}. Gray shade indicates the area with a winter surface density greater than each isopycnal.

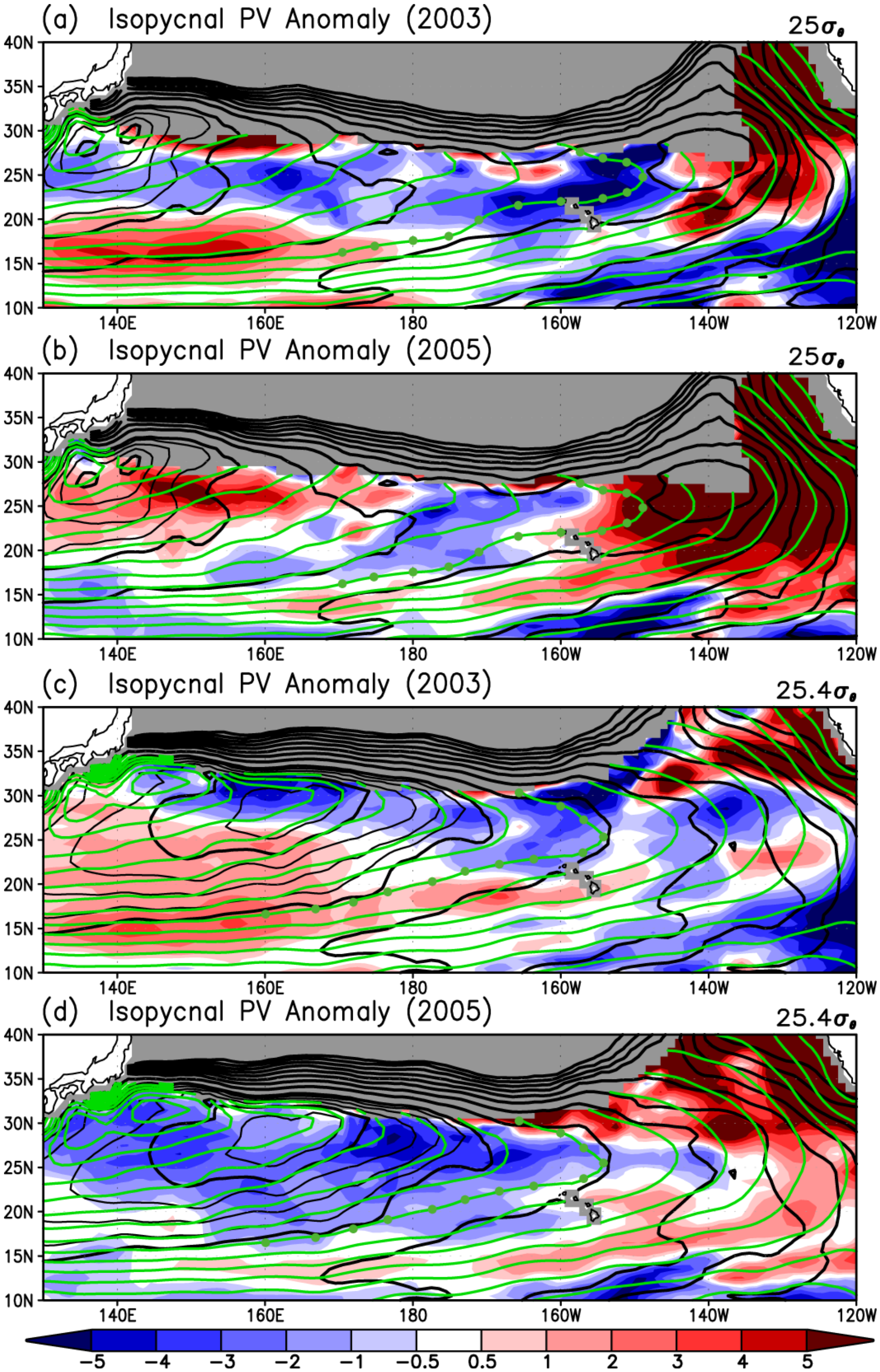

Figure 6. Yearly PV anomalies (color, unit is 10^{-10} $m^{-1}s^{-1}$) in (a) 2003 and (b) 2005 from the mean averaged from 2001 to 2008 at the 25.0 σ_θ surface based on the MOAA GPV. (c) and (d) are identical to (a) and (b), but at the 25.4 σ_θ

surface. Black and green contours show the mean PV and acceleration potential (m^2s^{-2}), respectively, averaged from 2001 to 2008. Gray shade indicates the area with winter surface density greater than each isopycnal.

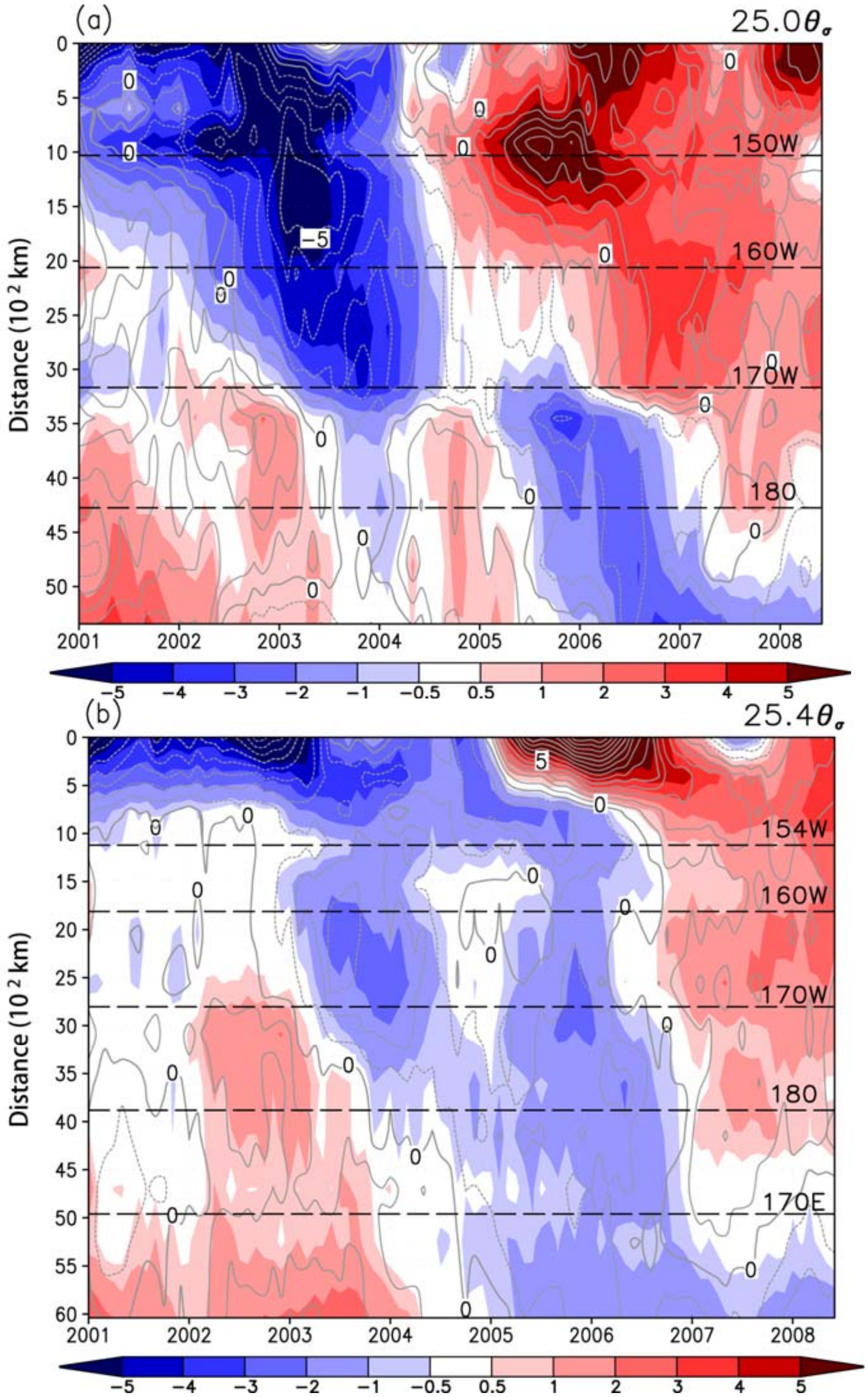

Figure 7. Time−distance plot of isopycnal PV anomaly (color, unit is 10^{-10} $m^{-1}s^{-1}$) along the isoline of acceleration potential with green dots in Fig. 5 and Fig. 6 at the (a) 25.0 σ_θ and (b) 25.4 σ_θ surfaces based on the MOAA GPV. Contour shows the anomaly of PV difference compared to 5° south (contour, unit is 10^{-10} $m^{-1}s^{-1}$). Contour interval is 10^{-10} $m^{-1}s^{-1}$. Vertical axis indicates the

distance (10^2 km) starting from the winter outcrop line. All variables are 13-month running mean values.

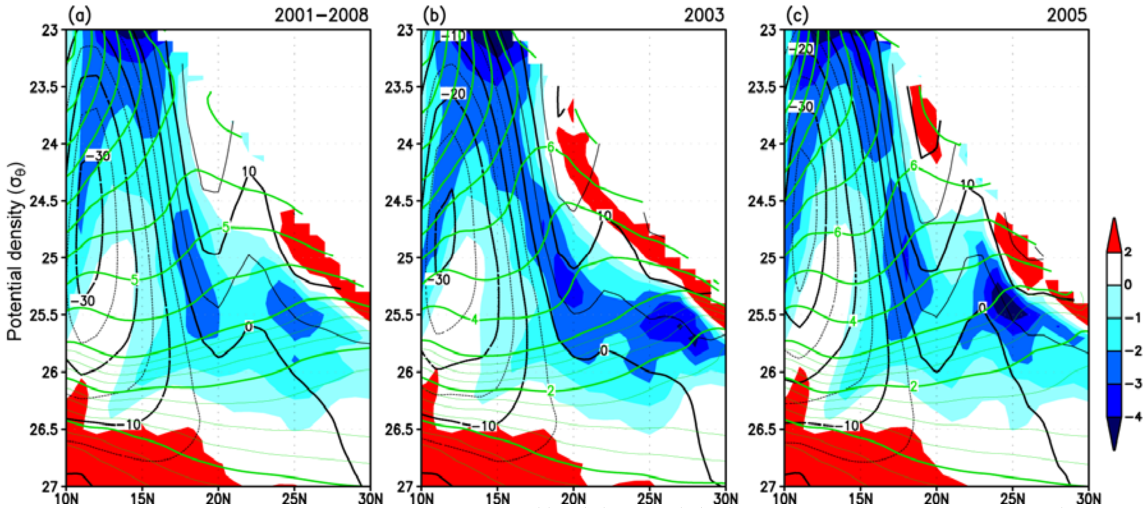

Figure 8. Meridional gradients of PV ($(f/q)(dq/dy)_\rho$) (color: unit is 10^{-11} $m^{-1}s^{-1}$) and of density ($d\rho/dy$) (black contour: unit is 10^{-7} $kg^{-1}m^{-4}$). Green contours show PV (10^{-10} $s^{-1}m^{-1}$) averaged between 180° and 165° W based on the MOAA GPV. (a) Mean averaged from 2001 to 2008 and annual mean in (b) 2003 and (c) 2005. Intervals of black and green contours are 5×10^{-7} $kg^{-1}m^{-4}$ and 10^{-10} $s^{-1}m^{-1}$, respectively.

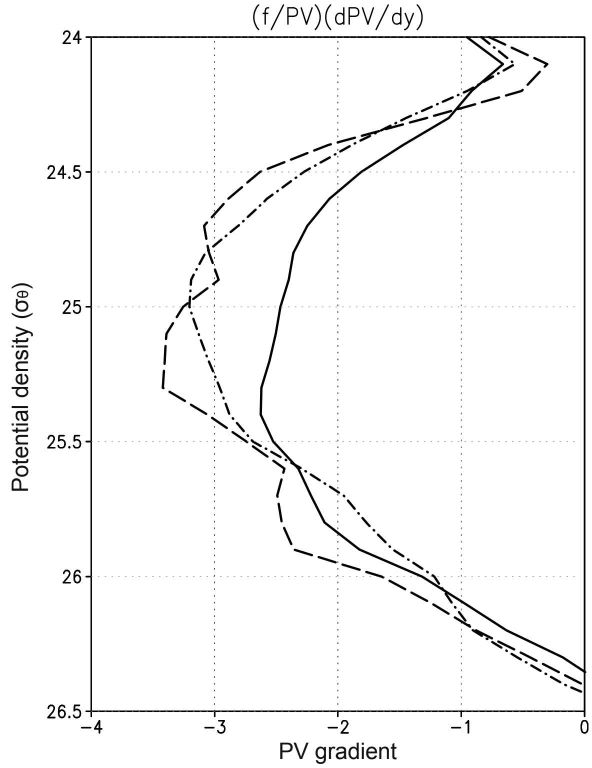

Figure 9. Minimum meridional PV gradients ($(f/q)(dq/dy)_\rho$) (unit is 10^{-11} $m^{-1}s^{-1}$) between 18° N and 21° N averaged between 180° and 165° W based on the MOAA GPV. Mean averaged from 2001 to 2008 (solid line) and annual means in 2003 (dash line) and 2005 (dash-dot line).

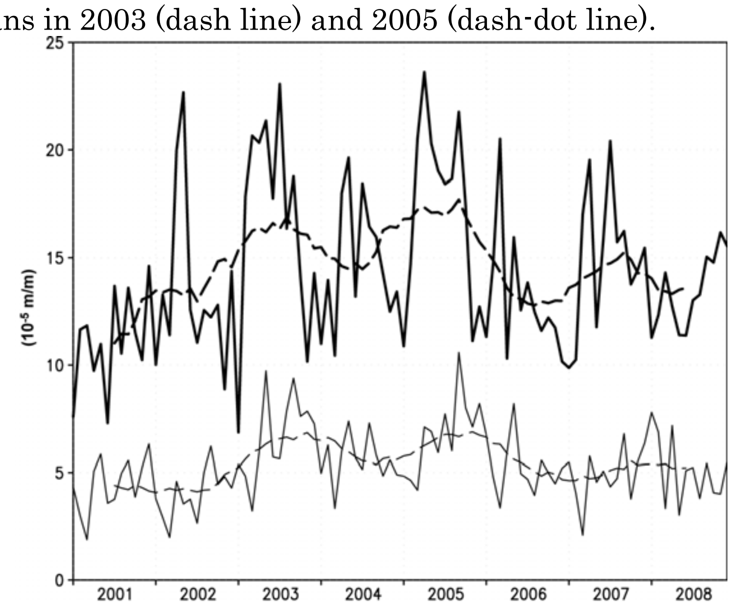

Figure 10. Maximum meridional slope between 18° N and 21° N at the 24.2 σ_θ surface averaged between 180° and 165° W based on the monthly MOAA GPV (thick curve, unit is 10^{-5} m/m). Thin curve shows the integral of

meridional PV gradients $((f/q^2)(dq/dy)_\rho)/\rho_0$ from the 24.5 σ_θ to 25.5 σ_θ surface (10^{-5} m/m). Dash curve indicates 13 month running mean.

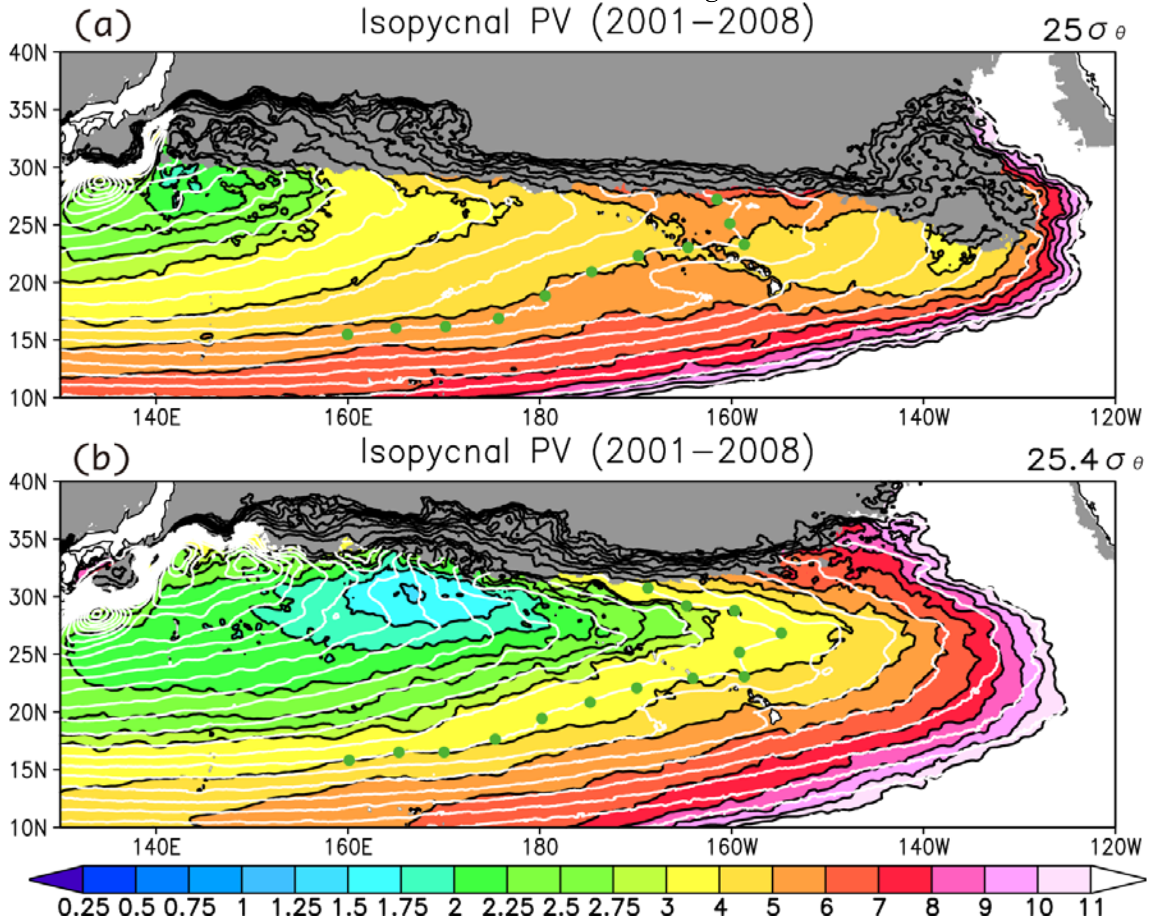

Figure 11. Same as Fig.5, but based on the OFES hindcast simulation.

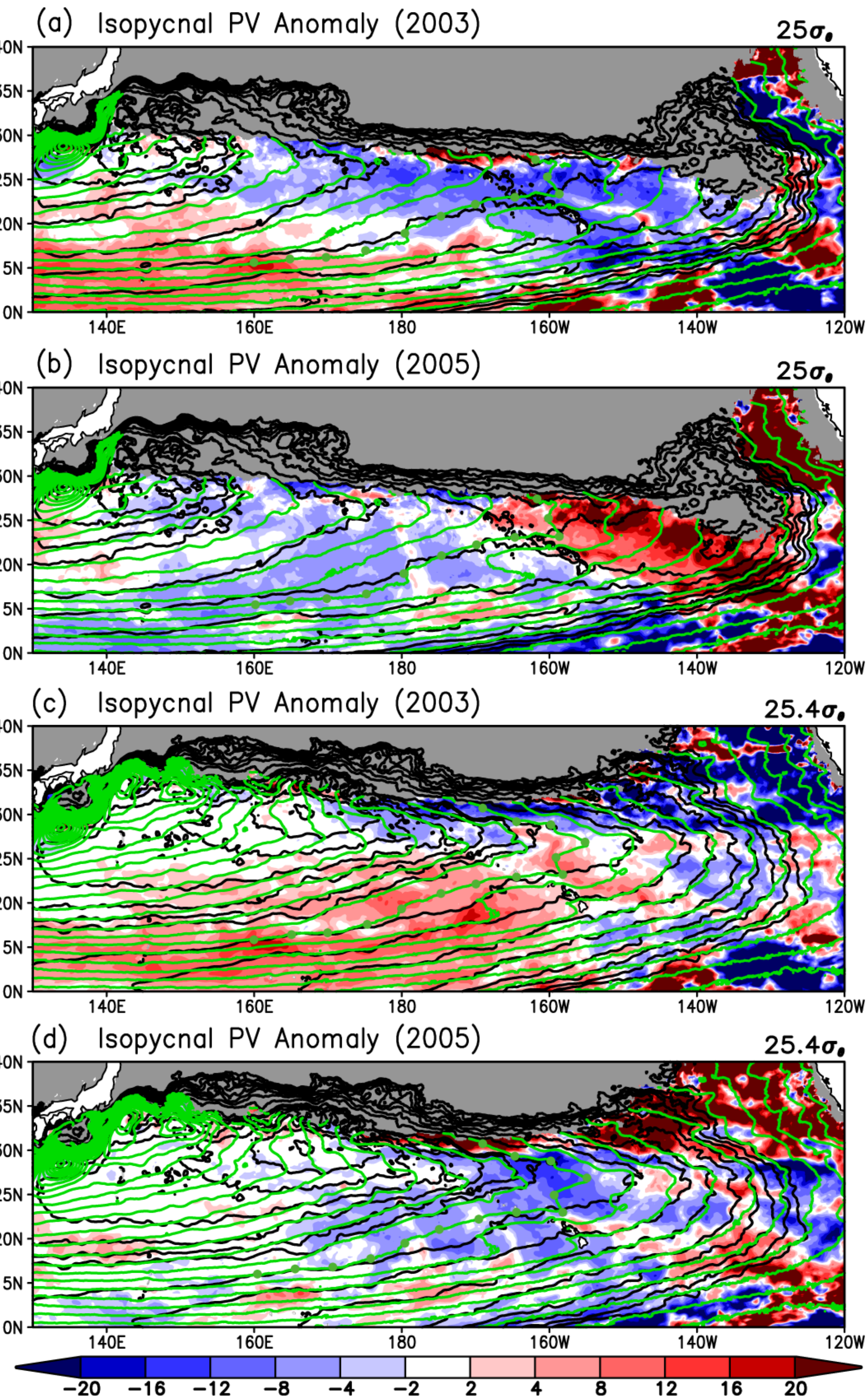

(a) Isopycnal PV Anomaly (2003)
$25\sigma_\theta$
(b) Isopycnal PV Anomaly (2005)
$25\sigma_\theta$
(c) Isopycnal PV Anomaly (2003)
$25.4\sigma_\theta$
(d) Isopycnal PV Anomaly (2005)
$25.4\sigma_\theta$
40N
35N
30N
25N
20N
15N
10N
140E
160E
180
160W
140W
120W
−20
−16
−12
−8
−4
−2
2
4
8
12
16
20

Figure 12. Same as Fig.6, but based on the OFES hindcast simulation. Note that the color scale is different from that in Fig.6.

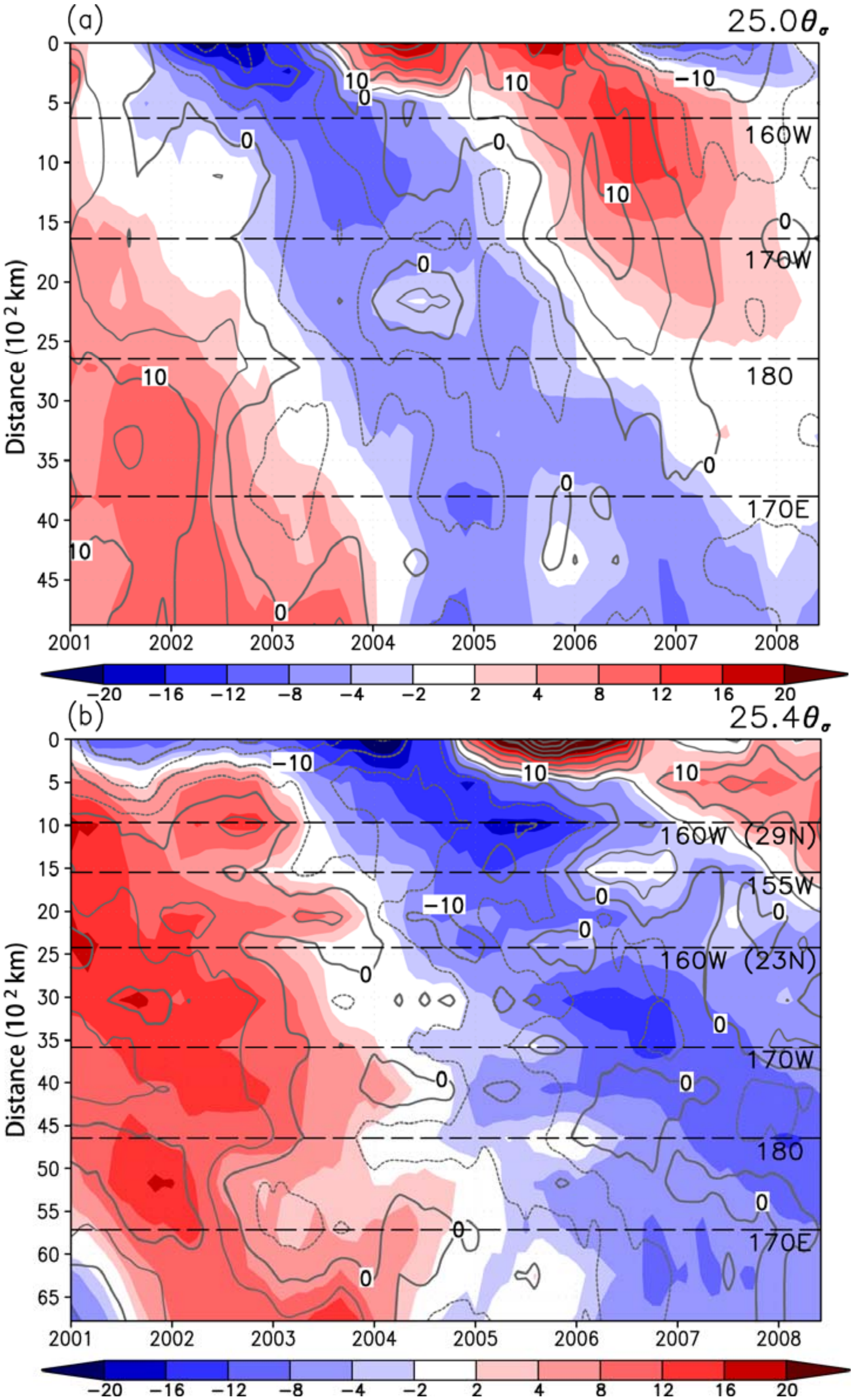
(a)
25.0θ_σ
160W
170W
180
170E
Distance (10 2 km)
(b)
25.4θ_σ
160W (29N)
155W
160W (23N)
170W
180
170E
Distance (10 2 km)
2001
2002
2003
2004
2005
2006
2007
2008
−20 −16 −12 −8 −4 −2 2 4 8 12 16 20

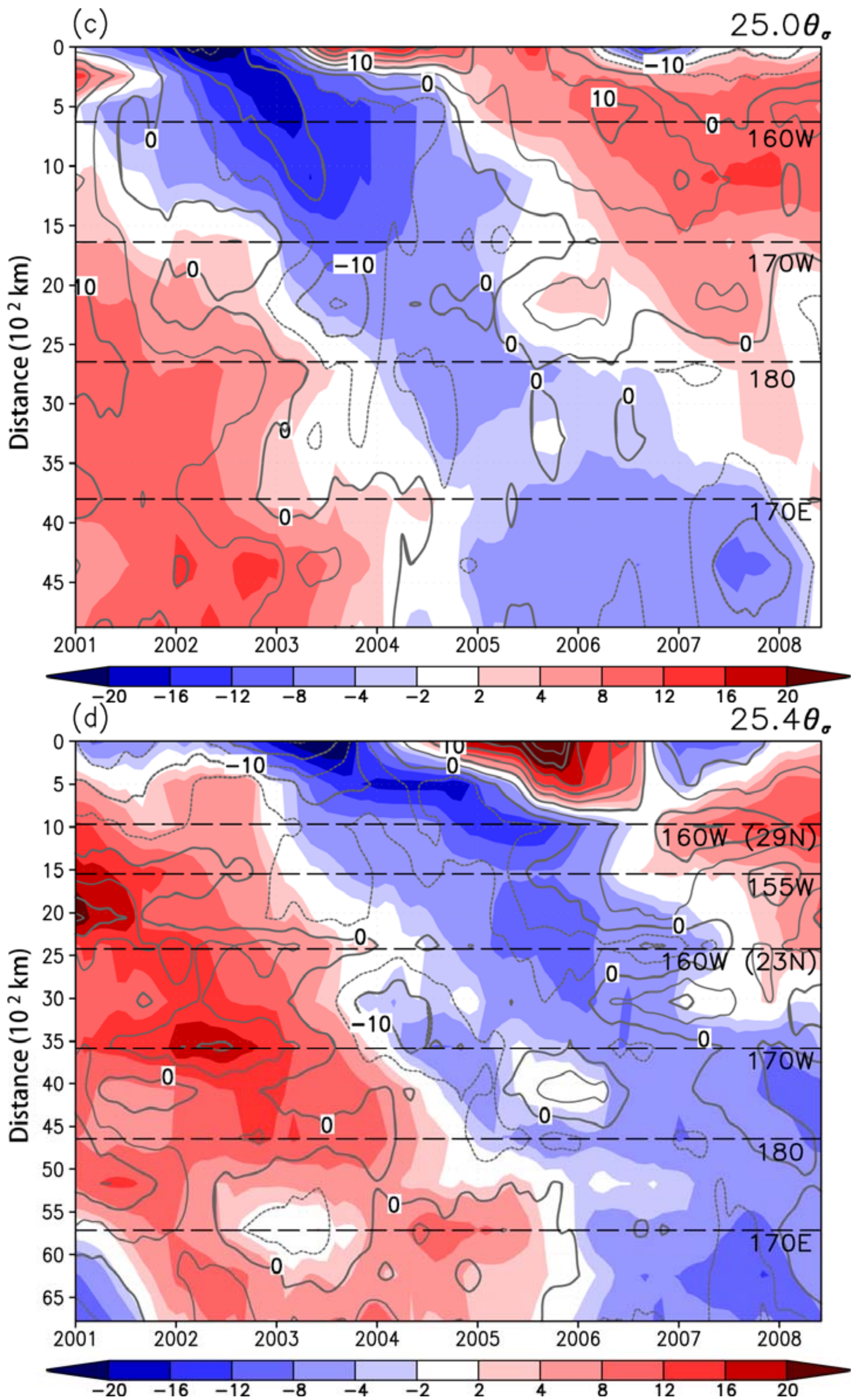

Figure 13. (a, b) Same as Fig. 7 but based on the OFES hindcast simulation. Vertical axis indicates distance along the acceleration potential with green dots starting from the outcrop line (Fig. 11). (c, d) Based on OFES sensitivity

simulation. Note that the color scale is different from that in Fig. 7 and the contour intervals is 5×10^{-10} $m^{-1}s^{-1}$.

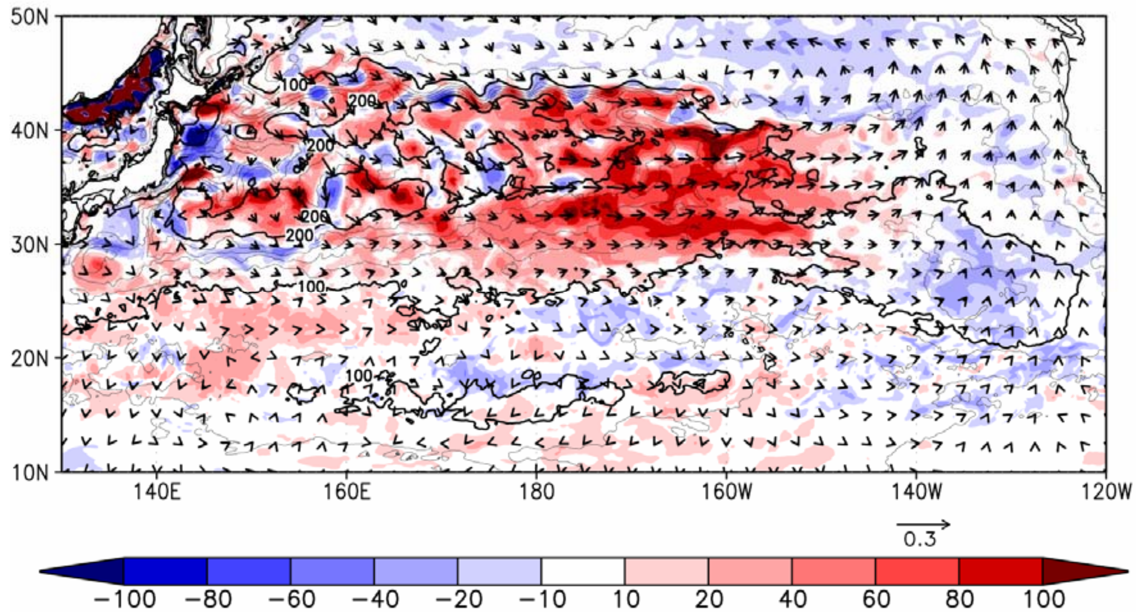

Figure 14. Winter (from January to March) mixed-layer depth anomaly (color, unit is m) in 2003 based on the OFES hindcast simulation. Contours indicate the mean winter mixed-layer depth averaged from 2001 to 2008. The thick (thin) contour intervals are 100 m (20 m). Vectors represent anomalies of winter wind stress (N m^{-2}). The mixed layer depth is defined as the depth at which the potential density differes from the sea surface density by 0.125 σ_θ.